Comparison of Regional Clear-Sky Albedos Inferred from Satellite Observations and Model Computations

B. P. BRIEGLEB,* P. MINNIS,** V. RAMANATHAN,* AND E. HARRISON*

*National Center for Atmospheric Research, Boulder, CO 80307***
**Atmospheric Sciences Division, NASA Langley Research Center, Hampton, VA 23665*

(Manuscript received 18 August 1984, in final form 20 August 1985)

ABSTRACT

We have taken an important first step in validating climate models by comparing model and satellite inferred clear sky TOA (top-of-atmosphere) albedos. Model albedos were computed on a 1° × 1° latitude–longitude grid, allowing for variations in surface vegetation type, solar zenith angle, orography, spectral absorption/scattering at surface and within the atmosphere. Observed albedos were inferred from GOES-2 minimum narrowband (0.55–0.75 μm) brightness for November 1978 over South America and most of North America and adjacent ocean regions. Comparisons of TOA albedos over ocean agree within ±1% (the unit for albedo is in percent and the differences in percent denote absolute differences), and thus lie within both theoretical uncertainties (due to water vapor and aerosol concentrations, and ocean surface spectral reflectivity), as well as observational uncertainties. The ocean comparisons also show significant latitudinal variations in both model and observations. Albedos over land mostly agree within ±2% for the entire range of significant geographical variation of albedo from 13% over the Amazon Basin to 24% over mountains of western North America. These agreements lie within both theoretical uncertainties (due to surface type and spectral/zenith angle dependencies), as well as observational uncertainties (due to spectral and angular conversions of observed brightness to broadband albedos).

1. Introduction

Clear-sky albedo is an important climate variable that determines not only the absorbed solar radiation under cloudless conditions, but also the role of clouds in modulating the solar radiation budget of the Earth–atmosphere system. For example, the effect of clouds on the solar energy absorbed by the surface-atmosphere system over a given region is simply proportional to the difference between the clear-sky albedo and the albedo of the region with clouds of any arbitrary vertical distribution. Hence, an accurate determination of the clear-sky albedo is a crucial requirement for climate studies.

Accurate estimates of clear-sky albedos, either from model computations or from satellite observations, although conceptually straightforward, are quite complicated and cause numerous practical difficulties. Clear-sky albedo is governed by the radiative interactions between atmospheric absorption and scattering, and surface-reflection features which vary with wavelength and solar zenith angle. For example, the strong spectral dependence of land surface reflectivity is governed by soil characteristics, vegetation types, and morphology (i.e., orientation with respect to the sun) which vary on spatial scales of the order of several hundred meters or less. Characterization of these features on the scale of several hundred kilometers poses a formidable challenge to climate modelers. (See Dickinson, 1983, for a more detailed discussion of the modeling of land surface reflectivity.)

Therefore, it is extremely important to validate the climate modeling practice of specifying bulk values of land reflectivities representative of regions of several hundred square kilometers or greater. This model validation is the primary objective of the present intercomparison study. The observed values used here are the clear-sky, broadband (0.2–4.5 μm) albedos inferred by Minnis and Harrison (1984c) from the visible (0.55–0.75 μm) channel instrument onboard the Geostationary Operational Environmental Satellite (GOES). The model calculations employ an improved version of the clear-sky radiative transfer model described in Briegleb and Ramanathan (1982).

The comparison study focuses on the region observed by GOES-2 between 45°S and 45°N, 30°W and 125°W. It is limited to the month of November. The choice of the region and the month is governed by the availability of the observational data. The selected regional location, however, covers most of North and South America and representative portions of the Atlantic and Pacific Oceans. It includes adequate samples of varied types of vegetation (forests, grassland, and shrubland), and surface conditions (ocean, swamps, wet soil, and desert conditions). Furthermore, the latitudinal variation of 45°N to 45°S is sufficient to cover many of the possible nonlinear interactions between

*** NCAR is sponsored by the National Science Foundation.

zenith angle dependence and spectral dependence of absorption and reflection.

2. Observed albedos

The observations used for comparison in this study are clear-sky albedos derived by Minnis and Harrison (1984c, hereafter MHc; see their Fig. 9) from GOES-2 visible count data. This dataset was chosen because it provides nearly complete, nonoverlapping spatial coverage of the viewed earth disc. As an imager, the GOES visible channel is nominally designed so that the area represented by each pixel is independent of, but contiguous with, the surrounding pixels. Thus, a complete image of the viewed earth disc is produced. The GOES data was also chosen because its relatively high spatial resolution (8 km) permits better isolation of clear-sky areas. Furthermore, although the visible channel on the GOES is not calibrated in terms of absolute radiant power, it is a fairly stable instrument capable of measuring relative brightness (Minnis and Harrison, 1984a, hereafter MHa).

The GOES-derived data raises two crucial issues related to estimating broadband albedo. The GOES visible channel measures *brightness* (proportional to the radiant power—see MHa) within a narrow band of the solar spectrum (0.55–0.75 μm). Furthermore, although a *radiance* can be estimated from the measurement, the albedo depends on the *radiant exitance,* i.e., the radiance contribution to the exitance integrated over the upper hemisphere. Earlier estimates of broadband albedo from visible (0.50–0.70 μm) radiances (e.g., Winston et al., 1978) assumed isotropic reflectance and equivalence between visible and broadband reflectance. However, observations with both aircraft-born radiometers (e.g., see Brennan, 1969) and with satellite-born radiometers (e.g., see Ruff et al., 1968) have shown that assuming isotropy in reflectance can lead to serious errors in estimated albedo. Also, the work of Kondratyev (1969) points out the importance of spectral variations in surface albedo and, therefore, in TOA clear sky radiances and albedo. Thus, in estimating the broadband albedo from the GOES visible count data, we account for anisotropy in the reflected radiance field and for differences between narrowband and broadband reflectances.

In order to clarify the impacts of the assumptions for anisotropy and spectral dependence, we start with a few basic definitions. For a particular region (defined by the spatial resolution of ~8 km) the broadband albedo is given by:

$$\alpha(\zeta) = \frac{M(\zeta)}{M_s \cos\zeta} \tag{1}$$

where M is the TOA broadband radiant exitance, ζ is the solar zenith angle, and M_s is the incident solar irradiance. Here M is defined as:

$$M(\zeta) = \int_0^{2\pi} \int_0^{\pi/2} L(\zeta, \theta, \phi) \cos\theta \, d\Omega \tag{2}$$

where L is the TOA broadband radiance; $d\Omega$ ($= \sin\theta d\theta d\phi$) is the differential element of solid angle; ζ is defined as above; θ and ϕ are the viewing zenith and relative azimuth angles respectively.

The TOA broadband radiance L itself is given by:

$$L(\zeta, \theta, \phi) = \int_{0.2\ \mu m}^{4.5\ \mu m} L_\lambda(\zeta, \theta, \phi)\, d\lambda \tag{3}$$

where L_λ is the spectral radiance and λ refers to wavelength.

The angular distribution of the radiance is in general a function of wavelength, and can be represented by a bidirectional radiance function:

$$R_\lambda(\zeta, \theta, \phi) = \frac{\pi L_\lambda(\zeta, \theta, \phi)}{M_\lambda(\zeta)} \tag{4}$$

where L_λ and M_λ (spectral radiant exitance) are related according to Eq. (2).

Finally, the broadband radiant exitance can also be defined by a spectrally integrated version of Eq. (4), rewritten as:

$$M(\zeta) = \frac{\pi L(\zeta, \theta, \phi)}{R(\zeta, \theta, \phi)} \tag{5}$$

where R is the broadband bidirectional radiance function.

An exact evaluation of Eq. (5) would provide the most accurate estimate of clear-sky albedo for a given region. Such an evaluation is impossible in practice, however, because of the limited opportunities for satellite observation of the instantaneous, complete radiance field over a given region under clear skies. Thus, evaluation of (5) requires the use of approximations. The following approximations were employed by MHc to estimate clear-sky albedos:

(1) The broadband radiance L can be estimated from:

$$L = NB(D^2) \tag{6}$$

where D^2 is the square of the observed GOES count or, alternatively, the brightness in the 0.55 to 0.75 μm region. The narrow-to-broadband conversion function, NB, which relates D^2 to the broadband radiance, L, is derived (for ocean and land separately) by correlating nearly simultaneous, colocated and co-angled Nimbus 7 ERB broadband (0.2–4.5 μm) radiances with D^2 (see Eq. 1a and 1b of MHc). More details of the derivation of these albedos can be found in MHc.

(2) The logical consequence of Eq. (6) is that the bidirectional function R can be obtained from D^2, i.e., Eq. (6) is used to obtain $L(\zeta, \theta, \phi)$ from $D^2(\zeta, \theta, \phi)$. Given a distribution of (6) as a function of ζ, θ, and ϕ, R is obtained from (5) after making use of (2). The above procedure yields a unique function of R for land

and ocean separately. Then, for any latitude and longitude, Eq. (5) is adopted to obtain M, where Eq. (6) is used to get L from the measured count.

These assumptions imply that a representative contribution to the broadband TOA radiance comes from the 0.55–0.75 μm spectral interval. While reflectivities for many surfaces have large spectral variation, in general, the visible reflectivities increase with increasing broadband reflectivity (see Table 2). Briegleb and Ramanathan (1982) showed that for oceans the TOA visible (0.50–0.70 μm) albedo can be nearly identical to the broadband albedo due to compensations between predominantly scattering ($\lambda < 0.50$ μm) and absorbing ($\lambda > 0.70$ μm) spectral regions. Therefore, a good correlation between visible and broadband radiance should exist, as was found by MHc.

The above assumptions also imply that the angular dependence of the visible radiance is representative of the entire spectrum. Over oceans, Rayleigh scattering plus Fresnel specular reflection of the direct solar beam off the ocean surface should dominate the angular dependence of the radiance, and these effects should not change significantly for wavelengths outside the 0.55–0.75 μm interval. Over land, near infrared ($\lambda > 0.75$ μm) surface reflectivities can be quite large compared to those in the visible 0.55–0.75 μm range (see Section 3), and thus the contribution of surface scattering to the TOA radiance for wavelengths outside the 0.55–0.75 μm interval may be considerable.

To investigate the existence of any surface-type dependent bias in NB and R of Eqs. (5) and (6), we compared GOES and Nimbus 7 ERB (N7) inferred albedos in the following manner: the albedo α from Eq. (1) was evaluated using GOES counts and N7 radiances in Eq. (5) over those 250 × 250 km^2 regions where it was determined from MHb that the fractional cloudiness was less than 10%, making use of the bidirectional functions R from MHa. It was found necessary, because of the ~90 km resolution of each N7 scan spot, to ensure that at least 10 N7 samples within each 250 × 250 km^2 region were available, in order to provide spatial coverage comparable to the GOES. Using the N7 radiances, we also evaluated the albedo by numerically summing Eq. (2). This albedo will be referred to as the "binned" albedo α_b; it is a direct measure of the N7 albedo, avoiding bidirectional functions. Most of the solid angle bins in the numerical summation of Eq. (2) were filled; an average of 11 radiances comprised the mean in each angular bin.

It was found that the average GOES values of α were within ±1% of the N7 values of α_b for both land and ocean regions as shown in Fig. 1. Cloud contamination and geographical constraints limited the number of solar zenith angle intervals available for comparison, however. Use of N7 data from all viewing angle intervals (all θ in Eq. 5, using bidirectional reflectance models) resulted in a 1% to 2% overestimate of the averaged

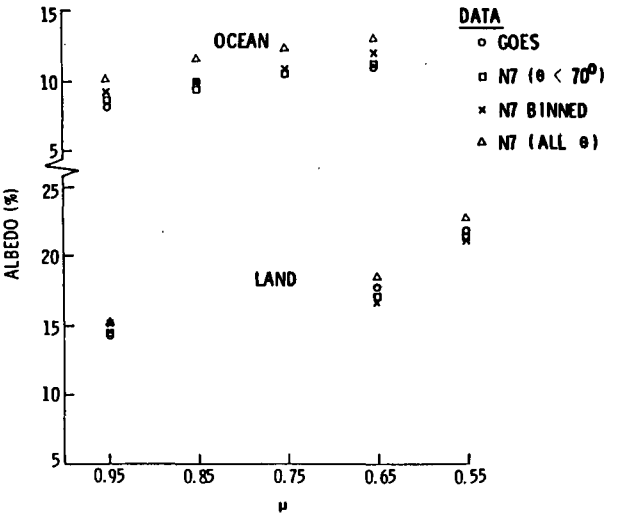

FIG. 1. Comparison of mean ocean and land clear-sky albedos derived from nearly simultaneous Nimbus 7 and GOES data for cloud fractions <10% during November 1978.

clear-sky albedo at a given value of ζ. This effect could result if the values of R are too low at $\theta > 70°$ and is similar to that seen by Arking and Vemury (1984). Albedos computed with N7 data for $\theta < 70°$ using the bidirectional reflectance models are within ±1% of the corresponding binned albedos α_b. Two conclusions may be drawn from these comparisons. First, the bidirectional models R applied to both the N7 and GOES radiances correctly account for the reflected anisotropies, on the average, for the viewing angles used here. Second, there appears to be no average bias in albedo resulting from the use of a single function NB for each surface category, ocean and land, to account for the spectral differences between GOES and N7.

Figure 2 shows the *regional* differences over land between albedos derived from GOES [Eq. (5)] and N7 (using bidirectional models of MHc) for cloud cover less than 10%. All values were computed from data taken near 1130 Local Time. Some values are the averages of data taken on more than one day while most were derived from only one pass of N7. Unshaded regions indicate nearly cloud-free data were not available from N7 between 16 and 30 November 1978. Use of radiances for totally cloud-free conditions would have severely restricted this comparison.

While the average difference over land is only −0.2% and the rms difference is 1.2%, some significant geographical patterns in the differences are readily apparent in Fig. 2. The GOES albedos over desert areas or shrubland (e.g., southern Andes and southwestern United States) are generally greater than the corresponding N7 albedos, while those over heavier vegetation, such as grasslands and forests, show a tendency to be less than the N7 values. The N7 and GOES albedos are equivalent over many coastal areas and those

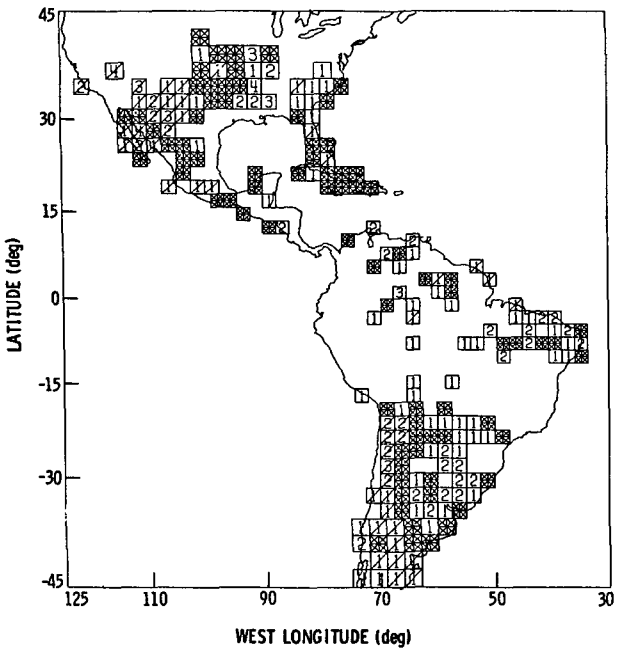

FIG. 2. Differences between nearly simultaneous Nimbus-7 and GOES-derived regional, broadband albedos in % for land area during November 1978 for cloud fractions <10%. (Shaded areas indicate differences within ±0.5%. Numbers with slashes indicate that Nimbus-7 values are less than GOES. Blank areas indicate nearly cloud-free data were not available.)

with a mix of shrub and heavier vegetation (transition zones). Most of these differences are based on instantaneous albedos which can be separated by up to half an hour and may be contaminated by cloud cover (which can vary in the time interval), so that some differences are expected in the results. The geographical grouping of differences of the same sign, however, strongly suggests that there are still some spectral and bidirectional reflectance variations with land-surface type which are unresolved in the GOES visible data. The differences in Fig. 2 may be the result of the regression formula for *NB* overcompensating over deserts and undercompensating over forests for the relative contributions of reflection in the near-infrared to the total albedo.

It may be concluded that the bidirectional models *R* and correlation formulas *NB* applied to the GOES data are good compromises between surface-type dependencies of spectral albedo. The conversion of GOES counts to TOA albedo results in a 2σ uncertainty of ±2% relative to N7 in regional clear-sky albedos over land, while over ocean the 2σ uncertainties in the GOES regional, clear-sky albedos are ±1%.

3. Computation of clear-sky albedos

a. Model

An improved version of the model described in Briegleb and Ramanathan (1982, hereafter BR) is adopted for this study. The solar spectrum is subdivided into four narrowbands: 0.2–0.5 μm, 0.5–0.7 μm, 0.7–0.85 μm, and 0.85–4.0 μm. These intervals were chosen for several reasons: 1) surface spectral reflectivities sharply increase for wavelengths longer than 0.7 μm, especially for vegetation; 2) atmospheric molecular scattering is very small longwave of 0.85 μm; 3) the approximate spectral response range of the GOES radiometer is 0.55–0.75 μm.

1) ATMOSPHERIC ABSORPTION/SCATTERING

The model includes absorption due to H_2O, CO_2, O_2, and O_3. Gaseous absorption is treated as in BR with the following changes. Oxygen is treated by the band model recently developed by Kiehl and Yamanouchi (1984) based on line-by-line calculations. The weak 0.72 and 0.81 μm H_2O bands are included explicitly in the 0.7–0.85 μm region as an addition to the Lacis and Hansen (1974) scheme adopted here for H_2O absorption. For each gas and narrowband, the gaseous absorption is assumed to occur in an absorption layer overlying the molecular and aerosol scattering layers.

Molecular and aerosol scattering are assumed to occur in two separate vertically and horizontally homogeneous layers. The layer optical properties are treated by the δ-Eddington formulation as re-derived in Coakley et al. [1983, Eqs. (B1) to (B8), (B12) and (B13)]. We used the layer-adding formulas of Coakley et al. [1983, Eqs. (1) and (2) for the direct beam, and Eqs. (B21) and (B22) for the diffuse beam] to account for multiple reflections between the atmospheric layers and the surface. Because of the strong wavelength dependence of Rayleigh optical depth, the scattering calculations are performed once every .04 μm interval between 0.2 and 0.85 μm.

To include the effects of tropospheric aerosols, we used the tropospheric aerosol model of Coakley et al. (1983, Table 4) over land, while over ocean we used their marine aerosol model (also his Table 4). Both of these aerosols have an extinction optical depth of 0.1 for wavelength 0.55 μm. Neither the tropospheric or marine aerosol of Coakley et al. (1983) have optical properties specified for wavelengths beyond 1 μm. Therefore, for wavelengths larger than 0.85 μm, we assume the optical properties to be independent of wavelength. For land, we used the following optical properties: $\tau = 0.05$, $\omega_0 = 0.90$, $g = 0.65$, where τ is the extinction optical depth, ω_0 is the single scattering albedo, g is the asymmetry factor. All of these parameters are needed to describe the reflectivity and transmission of the aerosol layer using δ-Eddington. For ocean we used the properties of $\tau = 0.08$, $\omega_0 = 0.98$, $g = 0.65$. The aerosol is assumed for both ocean and land to be a homogeneous layer underlying the homogeneous molecular scattering layer.

2) LAND SURFACES

The surface reflectivities are specified as a function of wavelength, for ten surface types (see Table 1). The prescribed surface reflectivities (see Table 2) are based on surface and aircraft observations (see BR). While 10 surface categories may seem unwarranted due to the limited number of observations available (see BR), there is a general progressive increase in broadband surface reflectivity from lowest to highest values. For example, if we order the types by 3 and 6 (evergreen forests), 7 (woodlands), 4 and 5 (mixed and deciduous forest), 2A primary (grassland), 2B secondary (shrubland), 8 secondary (rocky desert), and 8 primary (sandy desert), the reflectivities are ordered by 12, 15, 18, 20, 23, 30 and 43% respectively. Since our estimated uncertainty in these reflectivities is ±20% of value (this uncertainty is a guess, made by observing the range in the reported measurements summarized in BR), there is both reasonable separation in mean and overlap in uncertainty ranges. We conclude that using 10 surface categories is warranted.

It is well known that both vegetation and bare ground reflectivities have a strong spectral dependence. From the sources listed in BR, we have estimated narrowband spectral reflectivity for the 10 surface types. By ignoring the spectral dependence of the surface (i.e., using the estimated broadband albedo of Table 2 for each narrowband interval), errors in TOA broadband albedo of the order ±1% typically arise. Although this error is rather small, we conclude that the use of spectrally dependent surface reflectivity is warranted.

Satellite observations of the zenith angle dependence of TOA albedo over land surfaces (Taylor and Stowe, 1984) suggest that TOA albedo increases by about 20–30% of value as solar zenith angles range from 0° to 60°. Many surface observations (see Dickinson, 1983) show a strong zenith angle dependence of the surface albedo as well. We would thus expect that both the atmosphere and the surface contribute to the zenith angle dependence of the TOA albedo.

Land surface structure varies considerably among the surface types listed in Table 1. Attempts to model the surface albedo zenith angle dependence would therefore be very difficult. Our approach was to use the solar zenith angle dependence of the surface albedo given in Dickinson (1983), appropriate for a semi-infinite plant canopy consisting of randomly oriented leaves:

$$R(\mu) = R_0 \frac{(1 + d)}{1 + 2d\mu)} \tag{7}$$

TABLE 1. Land surface types.

Type	Description*	Components**	Fraction†	Matthews' vegetation type‡
1	Mixed farming, tall grassland	Cultivated ground, tall grassland	0.8	W (Cultivation intensity > 75%)
2A	Tall/medium grassland, evergreen shrubland	Grassland, shrubland	0.8	H, I, O, Q, R
2B	Short grassland, meadow and shrubland	Shrubland, grassland	0.8	J, L, P, S, T
3	Evergreen forest (needleleaved)	Forest, ground or rocks	0.9	4, 5, 7, 8
4	Mixed deciduous, evergreen forest	Deciduous, evergreen forest	0.5	A
5	Deciduous forest	Forest, bare ground	0.9	9, B
6	Tropical evergreen broadleaved forest	Forest, clearings	0.9	1, 2, 3
7	Medium/tall grassland, woodlands	Woodland, grassland	0.8	6, C, D, E, F, G, N
8	Desert	Sandy, rocky soils	0.5	U
9	Tundra	Tundra, bare ground	0.5	K, M

* These descriptions are an expanded version of those of Briegleb and Ramanathan (1982), for types 1, 2, 3, 6 and 7.

** Each type is considered to consist of 2 components. The primary component determines the type, but the secondary component (which may be the primary component of another type) is present to a varying degree.

† These fractions undoubtedly represent some regions, but in types which represent transition (2 and 7) or intrinsically variable regions (8), the fraction can range from 0 to 1.

‡ The association of Matthews' more detailed types and the types here was done both by using Matthews' description, as well as surface albedos (Matthews, private communication), and other observations—see Briegleb and Ramanathan (1982).

TABLE 2. Narrowband and broadband surface reflectivities (in % of incident solar irradiance at surface).*

Surface type	Narrowband in microns@,† 0.2–0.5	0.5–0.7	0.7–0.85	0.85–4.0	Broadband**
	(a) Primary surface component				
1	4	8	24	24	16
2A	5	10	30	30	20
2B	8	17	25	35	23
3	3	4	20	20	12
4	3	6	30	30	18
5	3	6	30	30	18
6	3	4	20	20	12
7	3	5	25	25	15
8	28	42	50	50	43
9	4	10	25	25	17
	(b) Secondary surface component				
1	5	10	30	30	20
2A	8	17	25	35	23
2B	5	10	30	30	20
3	5	10	15	22	14
4	3	4	20	20	12
5	7	13	19	28	18
6	5	10	15	22	14
7	5	10	30	30	20
8	15	25	35	40	30
9	7	13	19	28	18

* These surface reflectivities are assumed to be valid for 60° solar zenith angle.

@ The narrowband reflectivities are slightly modified (in a few instances) compared to Briegleb and Ramanathan (1982).

† Note that these narrowband reflectivities are uncertain by an estimated ±20% of value. For example, the 0.85–4.0 μm reflectivity over type 3 primary component is 20% ± 4%. (Note, an uncertainty of 20% for each narrowband yields an uncertainty of 2% in the computed TOA albedo).

** The broadband (spectrally integrated) reflectivities, calculated using the TOA solar irradiance fraction, are shown for reference purposes only. The model computations, however, employ only the narrowband reflectivities.

where μ is the cosine of the solar zenith angle, and R_0 is the reflectivity for $\mu = 0.5$ given in Table 2. Although some surfaces do not have plant canopies that fit the above assumptions (short grassland and desert of course), the expression is a function of only one empirical parameter d. We used the measurements of zenith angle dependence given in BR to determine the value of d for various surfaces, and arrived at 0.4 for arable land, grassland, and desert, and 0.1 for all other types.

If the surface zenith angle dependence is ignored (i.e., $\mu = 0.5$ value is used for all solar zenith angles) our model variation of the TOA albedo from 0° to 60° solar zenith angle is only about 10% of value, rather than the ~30% of value observed. Hence, we can justify the use of Eq. (7) for the zenith angle dependence.

3) OCEAN SURFACES

Over oceans, we have used Payne (1972) as a primary source of observed broadband surface albedos. Payne measured the broadband albedo due to both direct and diffuse downward irradiance above an ocean surface. In BR we used Payne's measurements for clear sky to represent the *direct* ocean surface albedo, even though the measurements contained a diffuse component to the downward irradiance at the surface. To represent more realistically the ocean surface albedo to *direct* solar radiation, we now use Payne's values (his Table 1 for atmospheric transmission $T = 1.0$), which implicitly remove the dependence of albedo on the diffuse component. We have fit Payne's tabulated values to within ±0.3% by the following expression:

$$\alpha(\mu) = \frac{2.6}{(\mu^{1.7} + 0.065)} + 15.0(\mu - 0.1)(\mu - 0.5)(\mu - 1.0) \quad (8)$$

This expression yields a surface albedo of 2.5% for overhead sun, which is consistent with the calculations of Tanaka and Nakajima (1977) for ocean with pure water. However, it differs from that used in BR in that the high sun ($\mu > 0.5$) albedos are now lower by ~2%, while the low sun ($\mu < 0.5$) albedos are now higher by up to ~5% for sun at the horizon. For diffuse downward irradiance, we have used Payne's value of 6.0%.

Ocean surface reflectivity depends not only on the intrinsic spectral reflectivity of the surface/bulk ocean itself, but also on the spectral dependence of the ratio of diffuse to direct irradiance from the atmosphere. Our model includes the later effect, since we explicitly calculate the direct and diffuse irradiance at the ocean surface.

Reflection of an incident beam of radiation from the ocean occurs either at the surface (Fresnel reflection) or by backscattering from the bulk ocean. The surface component has almost no spectral dependence because of the small variation of the index of refraction of water across most of the solar spectrum (see Paltridge and Platt, 1976, p. 292). The bulk component will have contributions both from water (Rayleigh scattering) and from hydrosols (suspended particulate matter, see Jerlov, 1968). We ignore the effects of hydrosols because their large space/time variability make it impossible to represent their effects.

Referring to the calculations of Tanaka and Nakajima (1977, Fig. 5), we note that even for pure water, the back scattering by the bulk ocean has a small spectral dependence. In Payne (1972) the broad band contribution of the bulk ocean back scattering is 0.5%. This back scattering contribution is already included

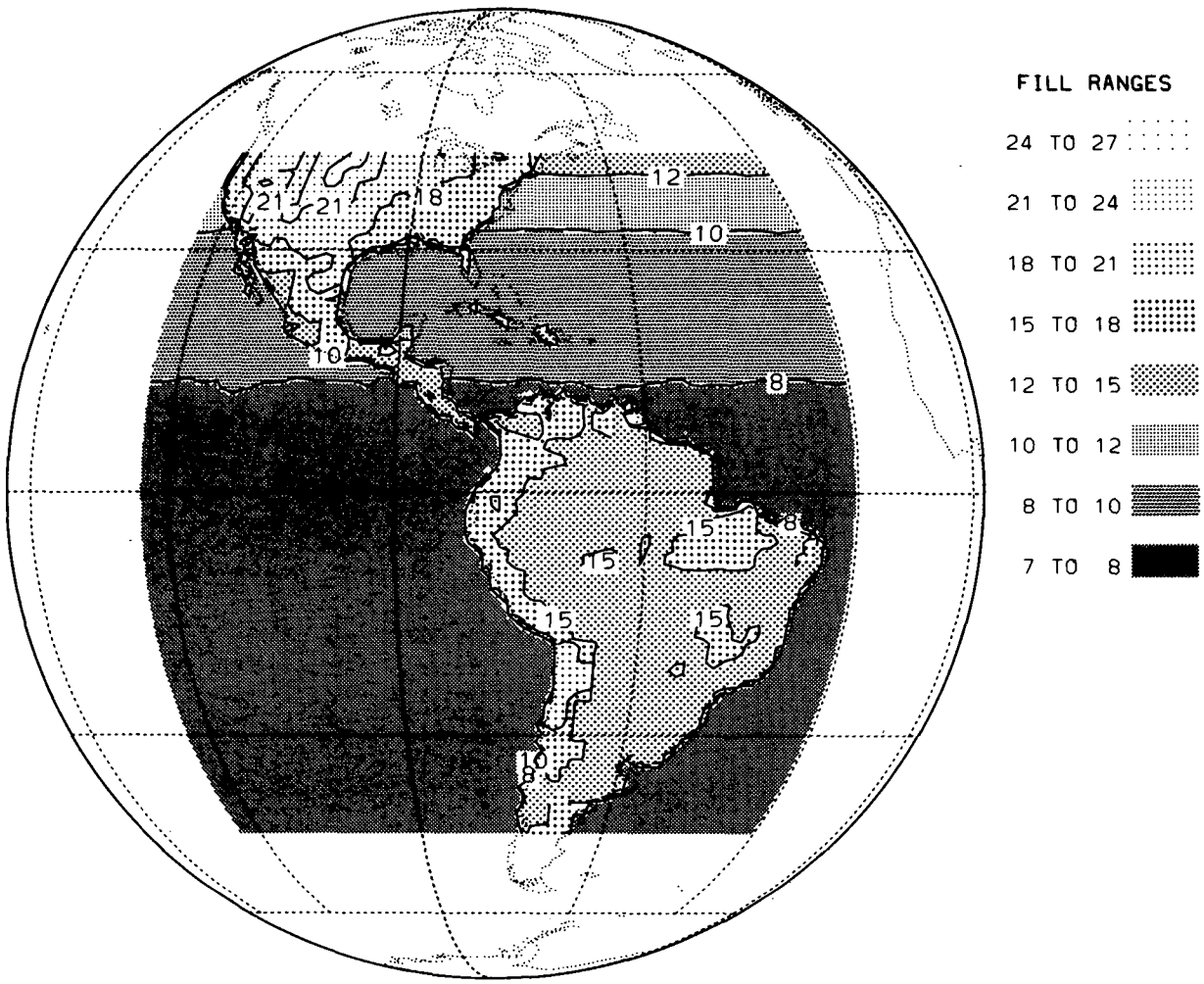

FIG. 3. Clear-sky albedos in % for local noon during November. (a) Observed values for 1978. (b) Computed.

in Eq. (8), but to determine the influence of its spectral dependence on the TOA albedo, we performed the following calculations.

The ocean spectral reflectivity was calculated using a two layer surface/bulk model of the ocean, where surface reflection is governed by Fresnel reflection and the bulk ocean Rayleigh reflection by δ-Eddington approximation. The optical properties of water were taken from tables in Paltridge and Platt (1976). Results suggested spectral corrections for the bulk ocean scattering of 2.0%, −0.3%, −0.7%, −0.7% for the 0.2–0.5 μm, 0.5–0.7 μm, 0.7–0.85 μm, and 0.85–4.0 μm spectral intervals respectively. We added these corrections to the diffuse ocean reflectivity of 6.0% and to the direct ocean albedo of Eq. (8), and performed model sensitivity calculations. The effect on the TOA broadband albedo was less than 0.05% for solar zenith angles from 0° to 85°. Therefore, we have neglected the intrinsic spectral dependence of ocean surface reflectivity.

b. Input data

The model calculations are performed on a 1° × 1° latitude/longitude grid to take advantage of the high resolution vegetation data of Matthews (1983). Matthews' 31 vegetation classifications were converted to the 10 categories given in Table 1.

Zonally symmetric, latitudinally dependent values of H_2O from Oort and Rasmussen (1971) are specified in these computations. Since their data are for the Northern hemisphere, November data are used for the northern hemisphere calculations and May data for the Southern Hemisphere calculations. Furthermore, a smooth function was fit to the observed latitudinal variations in the total H_2O amount since this is the only relevant parameter needed for the clear-sky calculations. The total column content of O_3 is specified as: $0.31 + 0.1 \sin(\phi)$ in cm-stp, where ϕ is latitude. The uncertainties in the clear-sky TOA albedo due to

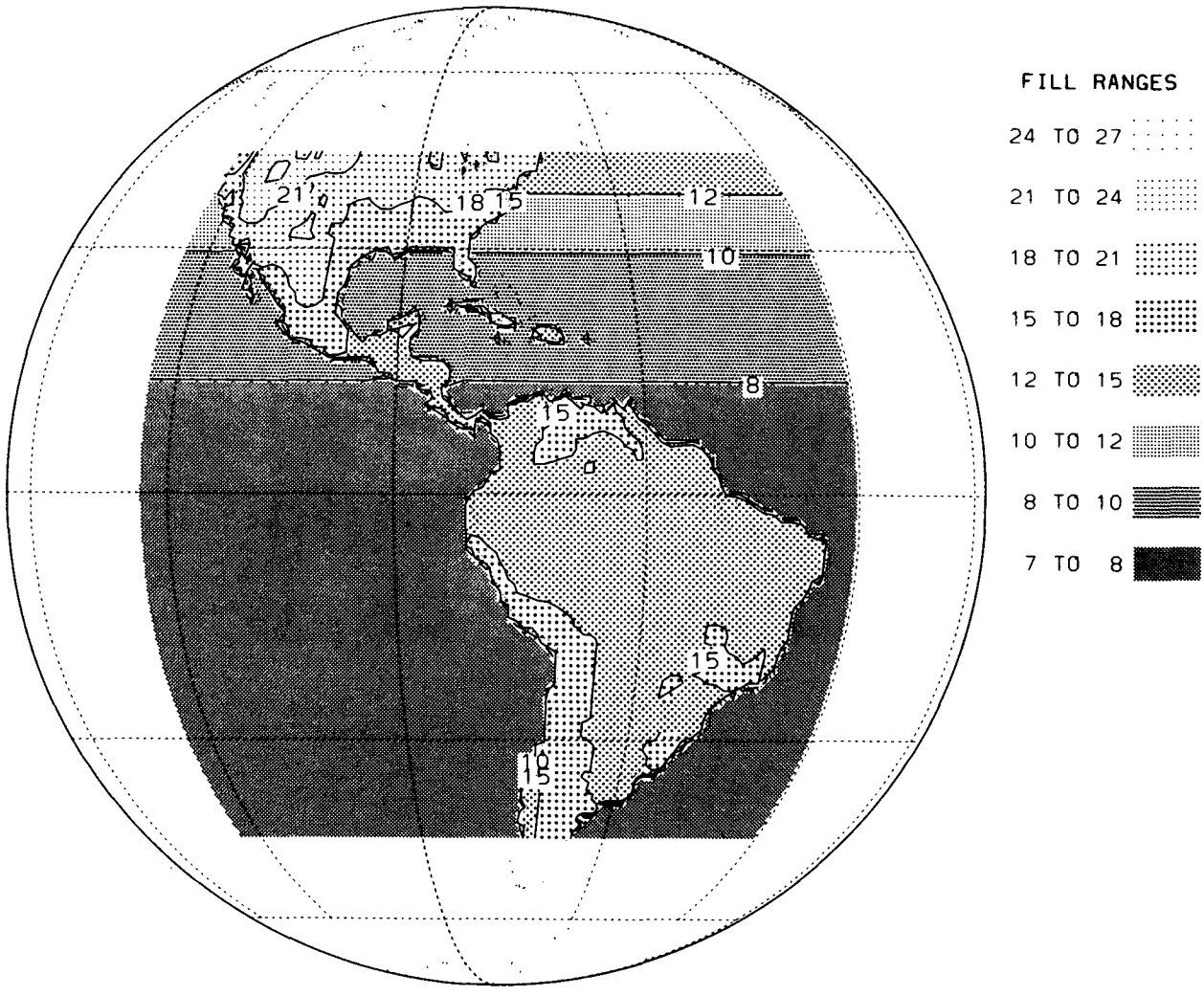

FIG. 3. (*Continued*)

these simplified prescriptions of H_2O and O_3 are no more than 1%. Sensitivity calculations with the model, performed by multiplying the H_2O column content by 0.5 and 1.5 yielded changes of −0.5% and +1.0% respectively in TOA albedo. Similarly, multiplying the O_3 column content by 0.5 and 2.0 produced changes in TOA albedo of +0.2% and −0.3% respectively.

The surface orography was specified with the 1° × 1° mean height of the FNOC Terrain Data (1976). The elevation, through surface pressure, influences the Rayleigh optical depth and the column amount of water vapor. These effects have been approximated by scaling the column Rayleigh optical depth with a scale height of 8 km and the column H_2O with a scale height of 2 km. Sensitivity calculations with the model, performed for topography of about 5 km elevation, but allowing only the Rayleigh optical depth to vary, yielded a decrease in albedo typically 0.5%.

4. Results

The observed and computed values of local-noon clear-sky albedos are shown in Figs. 3a and 3b, respectively. Unlike the GOES-inferred albedos used in Section 2.0 to compare with N7 data, the values in Fig. 3a are based on minimum brightness, and hence are essentially cloud free. The differences between the two values are shown in Fig. 4. In order to highlight the main features of the regional patterns, the results are discussed below according to the major geographical divisions.

1) SOUTH AMERICA

The geographical patterns shown in Fig. 3 reveal the significant impact of the underlying vegetation on the

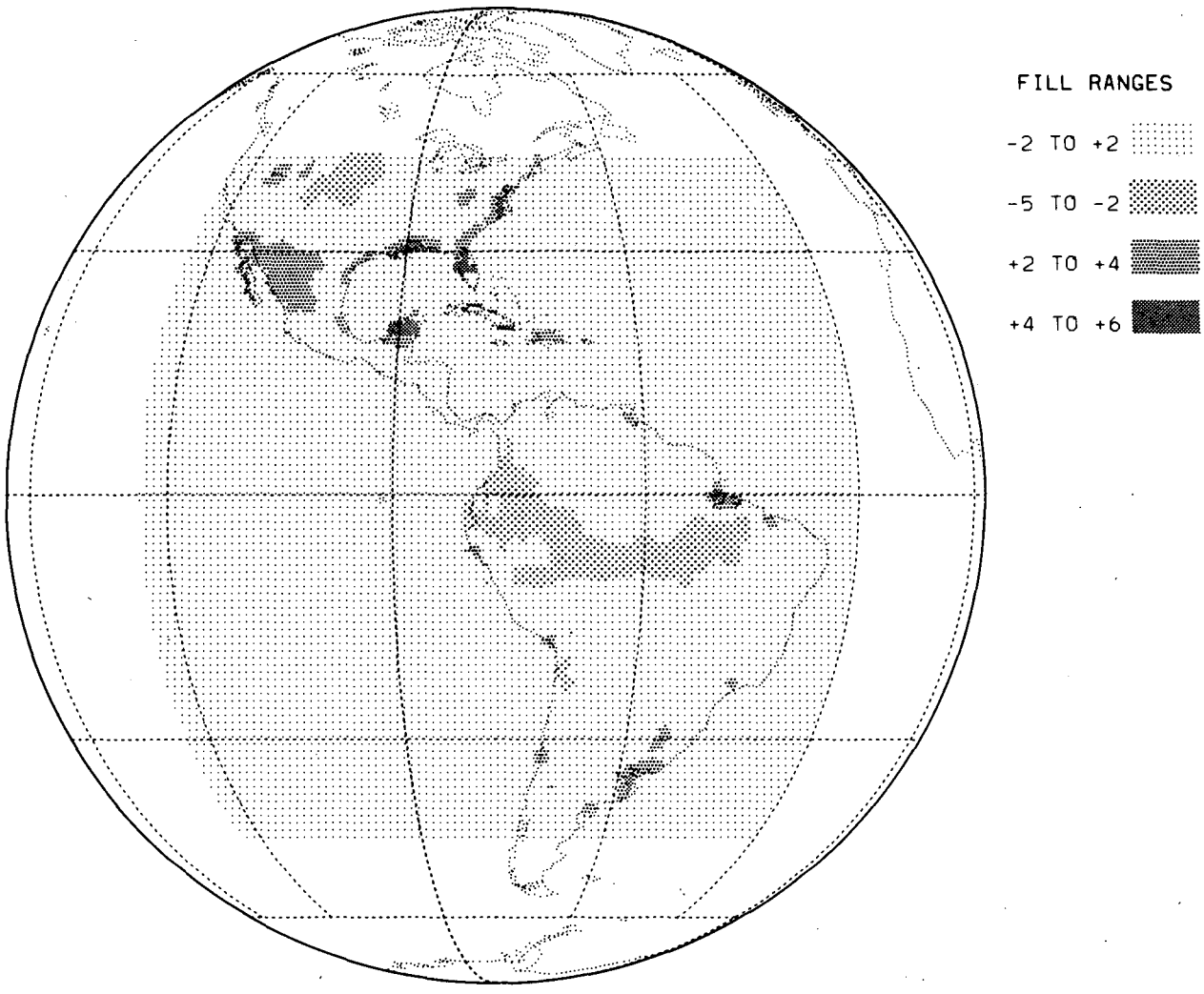

FIG. 4. Model minus observed clear-sky albedos (in %) from Fig. 3.

clear-sky TOA albedo (denoted by α for the subsequent discussions). It is noted that, for the same latitude, the albedos over land are larger than the oceanic values by factors ranging from 1.5 to 2.0. The regional variations of α within the land areas can be broadly categorized in terms of high-albedo ($\alpha > 15\%$) and low-albedo regions ($\alpha < 15\%$).

The high albedo regions are characterized by two distinctively different vegetation types. The first type includes short grass and shrubland accompanied by steppe and semi-desert conditions (northwest Argentina and Patagonia); mountain conditions (Andes); and savanna or no wood cover (Guiana Highlands including Guiana and eastern Venezuela). The second type encompasses dry forests and open woodlands of the northeast Brazilian highlands and the Parana–Paraguay basin which includes northern Argentina and Paraguay. The low albedo regions of South America are characterized by the rain forests of the Amazon Basin and the tall grasslands of Uruguay, southeastern Brazil, and the Argentinean pampas. The transition region between low and high albedos consists of mixed deciduous evergreen forests and grasslands.

The model computations are able to capture the geographical changes of clear-sky TOA albedo imposed by the variations in vegetation types with only a few minor exceptions. The magnitudes of the differences between model and observations are generally within ±2%. However, the model albedos over a portion of the Amazon Basin are more than 2% less than the observations, while the model results over eastern Argentina and Uruguay are more than 2% greater than the observations. The differences over Argentina and Uruguay may be attributed to soil moisture variations not taken into account by the model since these areas can be marshy at certain times of the year. The large dif-

ferences (>2%) over the Amazon Basin may be due to some residual cloud contamination in the observations since noon is the time of maximum cloud cover (mostly popcorn cumulus) in that area. The same result would also be found if the surface albedo specified in the model were too low.

Since the 2σ uncertainty in observed albedos is about ±2% (see Section 2 and Fig. 2) and the uncertainty in the model computations is about ±2% (see Table 2), no further attempts are made to explore the sources of the differences nor to fine tune the surface reflectivity parameterization in this study.

2) North America

There is an overall trend of poleward increase in the albedo. Furthermore, for the same vegetation type, the North American albedos are larger than the South American values by 3 to 6% (e.g., compare albedos over the Andes and just east of the Rockies, areas which have type-2B vegetation classification). The overall poleward increase in albedo within North America and the interhemispheric asymmetry in the albedo for the same vegetation type can be attributed to the zenith angle dependence of surface reflectivity and to Rayleigh scattering. The differences in the vegetation types, however, significantly influence the geographical variation in albedo.

Over the eastern U.S., the south-to-north increase of albedo from values close to 15% in the Gulf and Atlantic coastal plains to about 21% around 45°N is partly due to the change in the vegetation from deciduous forests with evergreen trees to cultivated farmland (see Table 2 for surface reflectivity). The only exception is the Great Lakes region (~45°N) where the albedos are slightly less than 15%. Within the interior plains, the westward increase in the albedo is due to the change in the vegetation from deciduous forests and cultivated lands of the midwestern United States to the grassland of the Great Plains. Further west, the albedos continue to increase as the vegetation type changes from grassland to shrubland; however, the elevation of the mountains contributes to the increase as well, as can be seen by the southward extension of the high albedo region >18% into Mexico. Model calculations reveal that the elevation of the mountains increases the clear-sky albedos by about 2% because of the diminished H_2O column content.

Overall, the model calculations are in good agreement with the observed values except for several important areas. In the eastern United States and northern Mexico, the 18% contour extends farther south in the model results than in the observations. In northern and central Mexico albedo differences in some locations are quite large (model albedos higher than observed by ~2 to 4%). This could be a result of the shrubland (type 2B in Table 1) vegetation classification for east-central Mexico, the same classification which is used for much of the southwest United States. The shrubland in this region might be more extensive than its U.S. counterpart, and may very well have surface albedos more like that of type 2A. The coniferous forests and grasslands in parts of the Rockies reduce albedos north of 35°N to less than 21%. The areal extent of this relatively low albedo region is not as pronounced in the observations as in the model computations. Some of the differences in this area may be due to snow cover. Minnis and Harrison (1984a), reported that some parts of this region were subjected to snow during November 1978 while snow was ignored in the model.

3) Oceans

For the same latitude belt, the clear-sky TOA albedos over ocean are significantly lower than over land (Figs. 3a and 3b). The main feature over ocean is the latitudinal variation of albedo. In order to examine the magnitude of that variation, the longitudinally averaged (between 30°W and 125°W) ocean TOA albedos are compared in Fig. 5. Since the clear-sky TOA albedos over ocean reported by Minnis and Harrison (1984c) and reproduced in Fig. 3a represent the minimum albedo conditions, a range of albedos drawn from their data set is shown as the shaded area in Fig. 5. The lower boundary of this area corresponds to the values

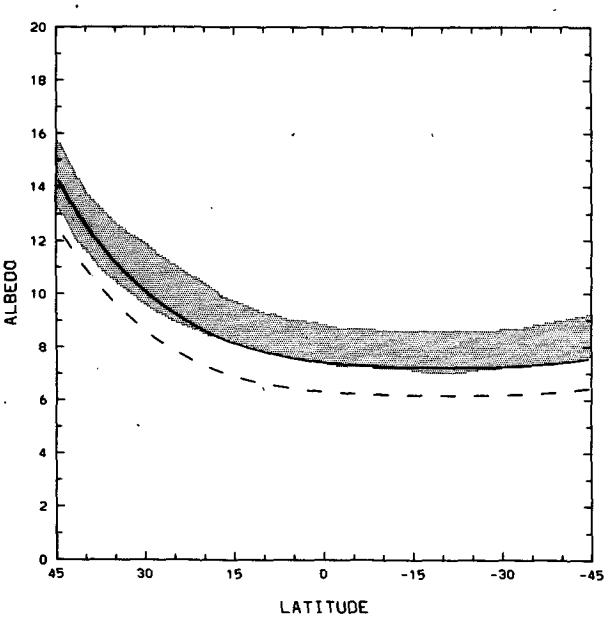

FIG. 5. Range of observed (shaded area) and computed clear-sky albedos for November at local noon over ocean. (Dashed line is for the aerosol-free case and solid line represents computations with aerosols.)

in Fig. 3a. The upper bound is derived from all instantaneous regional albedos for cloud cover <5%. The average cloud cover for those cases is only 1.3%, so that the contribution of clouds to the total albedo is ~0.5%. These results are taken to represent an upper limit to the clear-sky albedo over ocean.

A range of model results is also presented in Fig. 5. The lower curve represents the aerosol-free case, while the upper curve represents the marine aerosol (extinction optical depth of 0.1 for wavelength 0.55 μm; see section 3). The observed and computed albedos in Fig. 5 are in good agreement; the model albedos are only slightly lower than the observed range at all latitudes. Since the uncertainties in the satellite estimates are about ±1%, and the uncertainties in the model albedo from uncertainties in H_2O and O_3 concentrations are also about ±1%, no further exploration of the small differences between the mean observed and computed values is warranted.

In the model computations, the solar zenith angle variation of the ocean surface reflectivity and that of Rayleigh scattering contribute about equally to the latitudinal variation of the clear-sky albedo. The relative contributions of these effects may be seen in Fig. 6 which shows the results of model computations using a μ-independent ocean albedo of 6% (the value for diffuse solar irradiance) at all latitudes. For this case, the difference in the clear-sky albedo between 44°N and 18°S is 3.8%, which is roughly half of the value of 6.9% shown in Fig. 5.

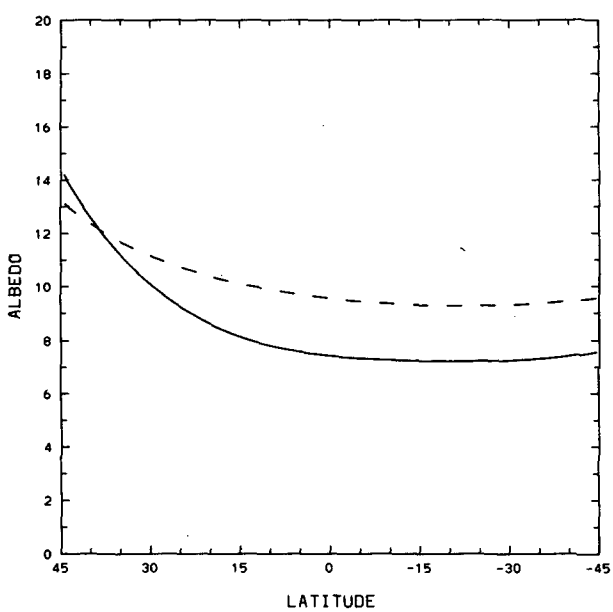

FIG. 6. Comparison of clear-sky albedos computed for solar-zenith angle dependent surface reflectivity (solid line) and for zenith angle independent surface reflectivity (dashed line) for November at local noon over ocean. (Solid line in this figure is identical to the solid line of Fig. 5.)

Spectral dependence of clear-sky albedo.

The differences between the computed visible, narrowband (0.5–0.7 μm) and the computed broadband (0.2–4.0 μm) albedos are shown in Fig. 7. Over the oceans, the difference is very small, because the enhancement of the albedo by Rayleigh scattering for wavelengths less than 0.5 μm very nearly compensates for the decrease in the albedo by H_2O absorption for wavelengths greater than 0.7 μm. Therefore, the visible albedo is a reasonable approximation to the total albedo. As shown in Fig. 7, however, this is not the case over the land because the strong spectral dependence of the vegetation reflectivity overwhelms the atmospheric effects. The visible albedo is smaller by about 2 to 6% than the broadband albedo because of chlorophyll absorption.

5. Concluding remarks

Comparison of clear-sky albedos computed with a model to those from satellite observations constitutes an independent verification of the model's treatment of atmospheric effects (parameterizations of theoretical formulations) and surface reflectivity (parameterized from surface and aircraft observations). By focusing on the regions of agreement between model computations and observations, it was possible to verify and interpret the following aspects of the model parameterization:

- Roughly 50% of the observed variation in clear-sky albedo over the ocean is due to the solar zenith-angle dependence of the ocean-surface reflectivity.
- The spectral dependence of the vegetation reflectivity has an important influence on the clear-sky albedo. The overall agreement in the geographical variation of the albedos indicates the importance of accounting for the spectral dependence of surface reflectivities.
- The observed and computed albedos show significant geographical/latitudinal variations which can be classified into three simple categories:

1) Broad-leaved (tropical rain) and needle-leaved (coniferous) evergreen forests and cultivated land have low clear-sky albedos.
2) Mountains, grassland, and shrublands have high clear-sky albedos.
3) Intermediate values of albedo are found over deciduous forests and tall grasslands.

- The zenith angle dependence of reflectivity over grassland was found to be important in producing the latitudinal variations in the albedo from South to North America.

Differences between the model and observational results within ±2% are considered to constitute good

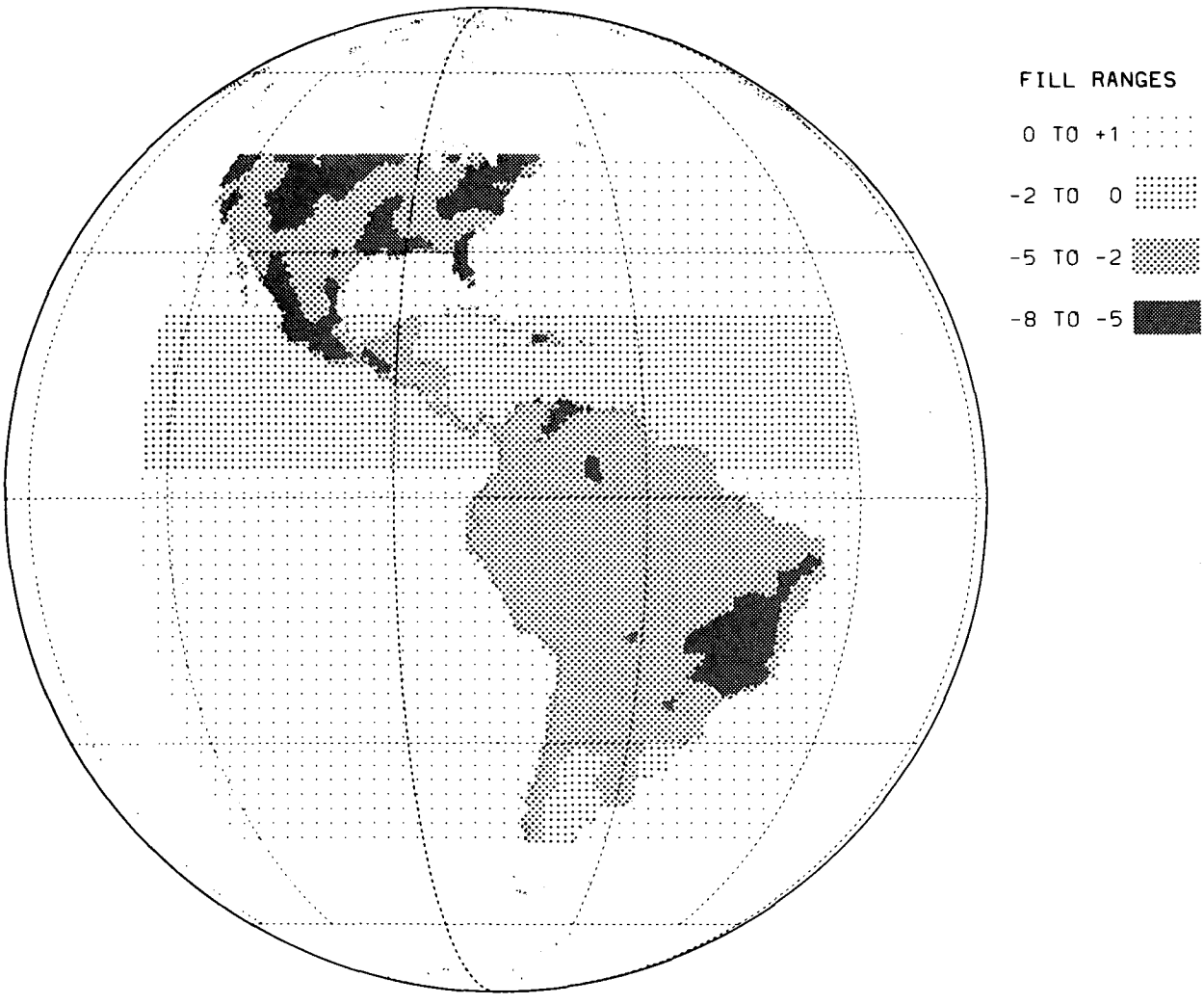

FIG. 7. Differences between computed visible and broadband clear-sky albedos (in %) at local noon for November.

agreement because they are within the 2σ uncertainty level of the observations. Also, the model does not take into account weather events which may cause fluctuations in surface albedo (e.g., soil moisture variations) and atmospheric turbidity, variables which may alter the clear-sky albedo by 1 to 2%. Explanations for differences >2% may be found either in the surface albedo specifications or in cloud contamination or spectral deficiencies in the observations. Further comparisons of albedos over areas of disagreement using observed and computed data from other seasons may help illuminate the sources of the discrepancies.

Acknowledgments. This work was supported in part by NASA-ERBE Grant L9477B, and was partly completed while V. Ramanathan was visiting NASA Research Center, whose hospitality is gratefully acknowledged.

REFERENCES

Arking, A., and S. Vemury, 1984: The NIMBUS 7 ERB data set: A critical analysis. *J. Geophys. Res.*, **89**, 5089–5097.

Briegleb, B. P., and V. Ramanathan, 1982: Spectral and diurnal variations in clear sky planetary albedo. *J. Climate Appl. Meteor.*, **21**, 1168–1171.

Brennen, B., 1969: Bidirectional reflectance measurements from an aircraft over natural earth surfaces. Goddard Space Flight Center, X-622-68-216, 82 pp.

Coakley, J. A., R. D. Cess and F. B. Yurevich, 1983: The effect of tropospheric aerosols on the Earth's radiation budget: A parameterization for climate models. *J. Atmos. Sci.*, **40**, 116–138.

Dickinson, R. E., 1983: Land surface processes and climate—Surface albedos and energy balance. *Advances in Geophysics*, **25**, 305–353.

Jacobowitz, H., H. V. Soule, H. Lee Kyle, F. B. House and the Nimbus 7 ERB Experiment Team, 1984: The Earth Radiation Budget (ERB) Experiment: An overview. *J. Geophys. Res.*, **89**, 5021–5038.

Jerlov, N. G., 1968: *Optical Oceanography*, Elsevier, 194 pp.

Kiehl, J. T., and T. Yamanouchi, 1984: A parameterization for ab-

sorption due to the A, B, and γ oxygen bands. *Tellus,* **37B,** 1–6.

Kondratyev, K. Ya., 1969: *Radiation in the Atmosphere,* Academic Press, 912 pp.

Kriebel, K. T., 1978: Measured spectral bidirectional reflectance properties of vegetated surfaces. *Appl. Opt.,* **17,** 253–259.

Lacis, A. A., and J. E. Hansen, 1974: A parameterization for the absorption of solar radiation in the Earth's atmosphere. *J. Atmos. Sci.,* **31,** 118–133.

Matthews, E., 1983: Global vegetation and land use: New high-resolution data bases for climate studies. *J. Climate Appl. Meteor.,* **22,** 474–487.

Minnis, P., and E. F. Harrison, 1984a: Diurnal variability of regional cloud and clear-sky radiative parameters derived from GOES data, Part I: Analysis method. *J. Climate Appl. Meteor.,* **23,** 993–1011.

——, and ——, 1984b: Diurnal variability of regional cloud and clear-sky radiative parameters derived from GOES data, Part II: November 1978 cloud distributions. *J. Climate Appl. Meteor.,* **23,** 1012–1031.

——, and ——, 1984c: Diurnal variability of regional cloud and clear-sky radiative parameters derived from GOES data, Part III: November 1978 radiative parameters. *J. Climate Appl. Meteor.,* **23,** 1032–1051.

Oort, A. H., and E. M. Rasmusson, 1971: Atmospheric circulation statistics. NOAA Prof. Paper No. 8, U.S. Govt. Printing Office, Washington, DC.

Paltridge, G. W., and C. M. Platt, 1976: *Radiative Processes in Meteorology and Climatology,* Elsevier, 318 pp.

Payne, R. E., 1972: Albedo of the sea surface. *J. Atmos. Sci.,* **29,** 959–970.

Plass, G. N., G. W. Kattawar and J. A. Guinn, Jr., 1975: Radiative transfer in the earth's atmosphere and ocean: influence of ocean waves. *Appl. Opt.,* **14,** No. 8, 1924–1936.

Ruff, I., R. Koffler, S. Fritz, J. S. Winston and P. K. Rao, 1968: Angular distribution of solar radiation reflected from clouds as determined from Tiros IV radiometer measurements. *J. Atmos. Sci.,* **25,** 323–332.

Taylor, V. R., and L. L. Stowe, 1984: Reflectance characteristics of uniform Earth and cloud surfaces. *J. Geophys. Res.,* **89,** (D4), 4987–4996.

Tanaka, M., and T. Nakajima, 1977: Effects of oceanic turbidity and index of refraction of hydrosols on the flux of solar radiation in the atmosphere-ocean system. *J. Quant. Spectrosc. Radiat. Transfer,* **18,** 93–111.

Salomonson, V. V., 1966: Anisotropy of Reflected Solar Radiation From Various Surfaces as Measured with an Aircraft-Mounted Radiometer. Research Report to NASA under contract NASr-147 2566-1/June 1966.

Terrain Data, 1976: Fleet Numerical Oceanography Center, Monterey, CA.

Winston, J. S., A. Gruber, T. I. Gray, Jr., M. S. Varnadore, C. L. Earnest and L. P. Mannello, 1979: Earth atmosphere budget analyses derived from NOAA satellite data June 1974–February 1978. Vols 1 and 2. NOAA-NESS, Washington, DC, 680 pp. [NTIS-N79-31862.]